All-Carbon Vertical van der Waals Heterostructures: Non-Destructive Functionalization of Graphene for Electronic Applications

*Mirosław Woszczyna, Andreas Winter, Miriam Grothe, Annika Willunat, Stefan Wundrack, Rainer Stosch, Thomas Weimann, Franz Ahlers, and Andrey Turchanin**

The functionalization of pristine graphene sheets is of key importance for their applications as electrical transducers in electronic devices such as, e.g., electric field-effect based nanosensors.[1,2] However, optimal routes to the functionalization have not been yet established which strongly restricts the applications.[3,4] As pristine graphene consists of exclusively sp^2-carbons organized in the honeycomb network, it is chemically relatively inert and difficult to functionalize via covalent bonding. Even when the covalent functionalization is achieved, due to associated structural modifications in graphene, its attractive electronic properties (e.g., high electrical charge mobility, strong ambipolar electric field effect, high thermal conductivity) are largely diminished.[1–3,5] Both covalent bonding to the graphene defects, as in oxidized graphene[6] or to graphene grain boundaries,[7] and direct bonding to the intact benzene rings[8] were studied and have demonstrated these limitations. In this respect, non-covalent functionalization of graphene, i.e. via weak van der Waals (vdW) forces, may provide an attractive alternative, as it does not induce severe changes into graphene.[4] Thus, the functionalization of graphene with flat polyaromatic molecules like porphyrins[9] has been shown. Although the adsorbed monolayers do not disrupt the graphene structure, their stability is low and limits implementations in devices. Therefore, a more durable functionalization of graphene based on the vdW interactions is highly desirable. Here we present a route to such functionalization via engineering of all-carbon vertical heterostructures by mechanical stacking[10] of amino-terminated carbon nanomembrane (NH_2-CNM) and single-layer graphene (SLG) sheets. CNMs are a novel two-dimensional (2D) carbon-based electronic material with dielectric properties made via electron-/photon-induced crosslinking of polycyclic aromatic self-assembled monolayers.[11,12] We employ SLG sheets, grown by low-pressure chemical vapor deposition (CVD) of methane on Cu foils,[13] and amino-terminated ~1 nm thick CNMs,[14–16] to assemble NH_2-CNM/SLG heterostructures on oxidized silicon wafers and use them for the fabrication of field-effect devices. The chemically active amino groups of NH_2-CNMs are located in these heterostructures in close vicinity to the graphene plane. We characterize structural, chemical and electronic properties of the large-area heterostructures and the fabricated electric-field devices by Raman spectroscopy, X-ray photoelectron spectroscopy (XPS) as well as by electric and electromagnetic transport measurements at room and low temperatures; and we study the electric field response of the devices in water. We show that the intrinsic electronic quality of pristine SLG sheets is preserved in the heterostructures, opening broad avenues for use in graphene-based electronic devices, e.g., for engineering electrical transducers for chemical and bio-sensing or as the complementary ultrathin dielectric material to SLG sheets for their integration with other materials.

A scheme for engineering the NH_2-CNM/SLG heterostructures on oxidized silicon wafers is presented in **Figure 1**. The process consists of two parallel routes including the fabrication of free-standing (i) NH_2-CNM and (ii) SLG sheets, which is finalized by their mechanical stacking into the vertical vdW heterostructure. To this end, NH_2-CNM sheets are prepared from self-assembled monolayers (SAMs) of 4′-nitro-1,1′-biphenyl-4-thiol on Au/mica substrates by electron irradiation (100 eV, 60 mC/cm^2) resulting in the lateral crosslinking of the biphenyl molecules[17] and the conversion of the terminal nitro groups into amino groups.[14,15] SLG sheets are grown by low-pressure CVD of methane on copper foils.[13] Then, the grown NH_2-CNM and SLG sheets are stacked on an oxidized highly doped silicon wafer by using the poly(methyl methacrylate) (PMMA) assisted transfer[18,19] (details in Supporting Information (SI)). In the formed heterostructure (see Figure 1, right), amino groups of the NH_2-CNMs are in close vicinity to the graphene plane, as they are separated from its surface by an only ~1 nm thick dielectric sheet of cross-linked biphenylthiols.[18] They can further be flexibly chemically functionalized for applications.[16,20]

Figure 2a shows an optical microscope image of the large-area NH_2-CNM/SLG heterostructure fabricated on an oxidized (oxide thickness ~300 nm) silicon wafer. Four different regions can clearly be recognized in this image corresponding to the bare substrate and the areas with NH_2-CNM, SLG, and NH_2-CNM/SLG heterostructure. As expected for the dielectric NH_2-CNM,[10] its optical contrast appears lower in comparison to the well-conducting SLG.[21] We employed Raman spectroscopy at ambient conditions to characterize graphene

Dr. M. Woszczyna, M. Grothe, S. Wundrack, Dr. R. Stosch, Dr. T. Weimann, Dr. F. Ahlers, PD Dr. A. Turchanin
Physikalisch-Technische Bundesanstalt
38116, Braunschweig, Germany
Tel.: +49–521–1065376
Fax: +49–521–1066002
E-mail: turchanin@physik.uni-bielefeld.de
A. Winter, A. Willunat, PD Dr. A. Turchanin
Faculty of Physics, University of Bielefeld
33615, Bielefeld, Germany

DOI: 10.1002/adma.201400948

© 2014 WILEY-VCH Verlag GmbH & Co. KGaA, Weinheim

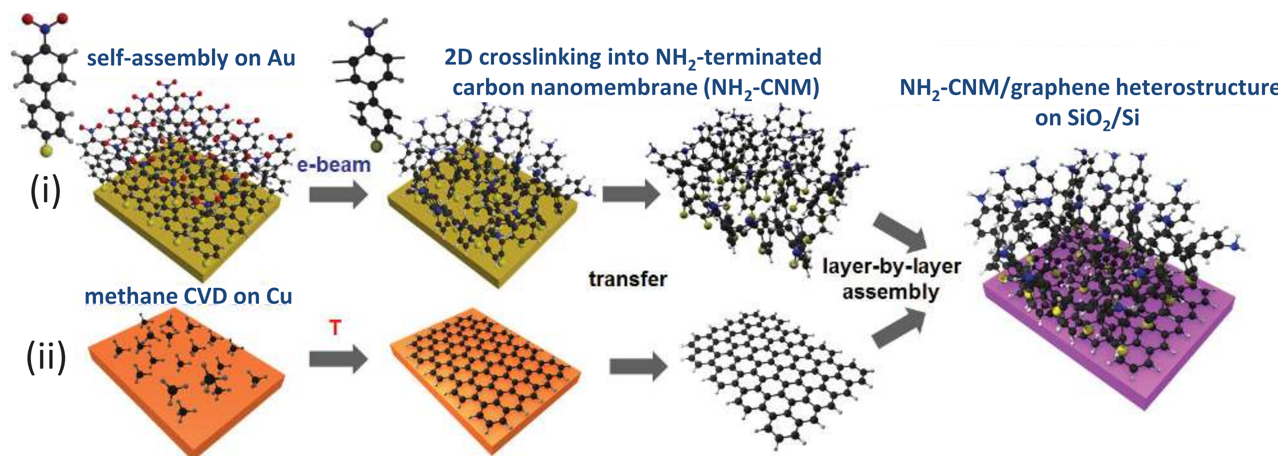

Figure 1. Scheme of the heterostructure assembly. In (i) amino-terminated carbon nanomembranes (NH_2-CNMs) are prepared from 4′-nitro-1,1′-biphenyl-4-thiol SAMs on Au/mica substrates by the electron irradiation induced crosslinking. In (ii) single-layer graphene (SLG) sheets are grown by CVD of methane on Cu foils. Finally, both types of sheets are separated from their original substrates and mechanically stacked to form the NH_2-CNMs/SLG heterostructure on an oxidized silicon wafer. Color code for atoms: black – carbon, grey – hydrogen, blue – nitrogen, yellow – sulfur, red – oxygen.

in different areas of this sample. As seen from Figure 2b, the intensity ratios between the characteristic D- and G- peaks of bare graphene and graphene integrated into the heterostructure are similar, which demonstrates that no additional structural defects are introduced into the SLG sheet upon stacking a NH_2-CNM on its top. Due to the disordered nature of NH_2-CNM and its monolayer thickness (~1nm), NH_2-CNM does not contribute of the measurable Raman intensity at our experimental conditions.[10] A detailed analysis of 15000 Raman spectra for both the bare SLG and NH_2-CNM/SLG heterostructure areas gave the same values for positions of G- and 2D- peaks, and for characteristic I(D)/I(G) and I(2D)/I(G) intensity ratios, which are 1589 cm^{-1}, 2680 cm^{-1}, 0.12 and 3.0, respectively (see Supporting Information (SI), SI Table 1 and SI Figure 1 for details). We have found that the standard deviation of the full width at half maximum (FWHM) value of the G-peak for SLG in the heterostructure (FWHM = 14.7 ± 1.3 cm^{-1}) is a factor of two lower than for the bare SLG (FWHM = 14.4 ± 2.5 cm^{-1}). This difference is indicative for a lower degree of charged impurities[22,23] in the NH_2-CNM/SLG heterostructure in comparison to the bare SLG on silicon oxide. The concentrations obtained by electric transport measurements (see next paragraph) correlate very well with the spectroscopy data.

Figure 2c presents high resolution XPS spectra of the core level S2p, C1s and N1s electrons of the heterostructure and the bare graphene regions. Due to the presence of NH_2-CNM, the S2p and N1s signals are clearly detected for the heterostructure region, in which also an increase by 0.6 eV of the C1s FWHM value in comparison to the bare graphene is detected. The N1s signal is composed of two components at 399.3 eV and 401.2 eV, which are characteristic for pristine ($-NH_2$) and protonated ($-NH_3^+$) amino groups,[14] respectively. As determined from attenuation of the substrate Si 2p signal (not shown) for the heterostructure and for the bare graphene, a NH_2-CNM contributes as expected with ~1.1 nm to the heterostructure thickness. A more detailed analysis of the XPS data is presented in SI Table 2. Thus, based on the spectroscopy characterization (Raman spectroscopy and XPS) we demonstrate that via the fabrication of the NH_2-CNM/SLG heterostructures terminal amino groups are brought in close vicinity of the SLG sheet (see Figure 1) without destroying its structural quality.

Next, we study by four-point measurements the transport characteristics of the SLG sheets integrated into heterostructures and compare them with the properties of bare graphene. To this end, a batch of large-area (140 µm × 25 µm) Hall bar devices with several side contacts (see **Figure 3**a) was fabricated from the same CVD grown SLG sheet placed on an oxidized silicon wafer. Then the wafer was sliced and a half of bare devices was directly examined, whereas on top of the second half a large-area NH_2-CNM was transferred to obtain heterostructure devices. In these devices, the NH_2-CNM covers both graphene areas and gold wiring with the bonding pads. Figure 3a presents an optical microscope image of one of the heterostructure devices. Raman mapping at positions of the characteristic D, G and 2D peaks (see Figure 3b) reveals its high structural quality and homogeneity on the large scale, which is directly confirmed by electric transport measurements. Figure 3c presents room temperature (RT) electric-field effect measurements as a function of back-gate voltage, U_{BG}, at four different side contacts of the device (see Figure 3a, P1-P4). As can be seen, the electrical characteristics are homogeneous on the scale of ~3500 µm^2. By keeping this device in high vacuum (~10^{-5} mbar) at RT we observed a shift of the graphene charge neutrality point (CNP) from initially 10 V to 3.5 V after pumping for 18 hours. Since possible contaminations, trapped between the SLG sheet and the silicon oxide substrate and/or between SLG and NH_2-CNM, cannot be removed by this treatment, we attribute this change to desorption of the environmental adsorbates or the remaining lithography-resist rests from the outer surface of the device.

Figure 3d presents a comparison of the mobility data for heterostructure (H) and bare graphene (G) devices as a function of charge carrier concentration. Prior to the measurements, all samples were kept at least for two hours in high vacuum (~10^{-5} mbar, RT). A striking difference is observed in the mobility data of H- and G-type devices. In the whole studied carrier concentration range (up to $n = 5 \times 10^{12}$ cm^{-2}) H-devices

© 2014 WILEY-VCH Verlag GmbH & Co. KGaA, Weinheim
Adv. Mater. 2014, DOI: 10.1002/adma.201400948

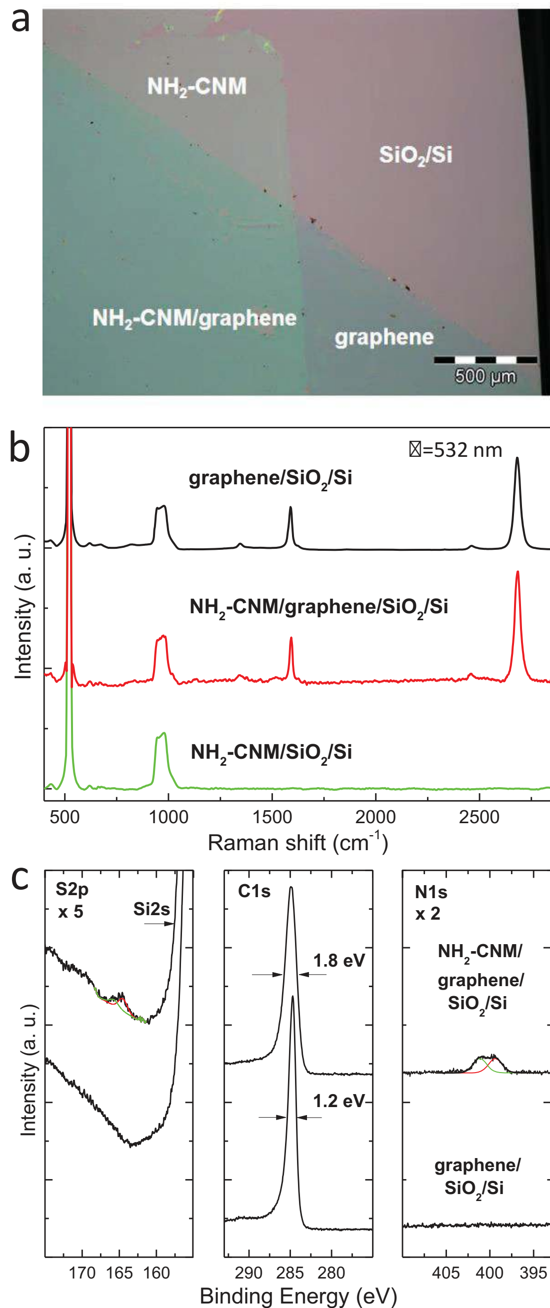

Figure 2. Characterization of structure and chemical composition of the heterostructure. a, Optical microscope image of the NH_2-CNMs/SLG heterostructure on an oxidized silicon wafer (300 nm oxide). Four different regions are recognized: bare SiO_2/Si; SLG; NH_2-CNMs; and NH_2-CNMs/SLG. The optical contrast was enhanced for better recognition. b, Raman spectra (λ = 532 nm) characteristic of the SLG, NH_2-CNMs and NH_2-CNMs/SLG areas. c, X-ray photoelectron spectroscopy (XPS) data of the characteristic S2p, C1s and N1s peaks for the bare SLG and the NH_2-CNMs/SLG areas. The terminal amino groups (see N1s) are detected on the surface of the heterostructure.

have a higher mobility than G-devices. Thus for a hole concentration of 2×10^{12} cm^{-2} (see Figure 3e) the mobility of G-devices is μ = 1000–1600 cm^2/Vs, whereas H-devices have a mobility increased by about 80%, μ = 2500–2640 cm^2/Vs. We selected two devices of each type with the highest mobility – H3 and G1 – and studied their transport characteristics in more detail. Figure 3f shows the RT conductivity plots, $\sigma = \rho^{-1}$, as a function of carrier concentration in the vicinity of respective charge neutrality points (U_{CNP} = 3.25 V for H3 and U_{CNP} = 8 V for G1). By measuring a deviation of $\sigma(n)$ from the linear behavior, we estimate a residual carrier concentration, n_*, for both devices, which gives a measure for the variation of local electrochemical potential due to the charged impurities at graphene interfaces, the so-called electron-hole puddles, which may result from trapped charges in the silicon oxide or adsorbates at the silicon oxide/graphene or graphene/environment interfaces.[23] In this carrier concentration range both holes and electrons participate in transport. The extracted n_* values are about 83×10^{10} cm^{-2} and 48×10^{10} cm^{-2} for G1 and H3 devices, respectively. These results are further confirmed by low-temperature measurements of the Hall coefficient, $R_H = \rho_{xy}/B\rho_{xx}$, in a magnetic field, B, of 1 T, where ρ_{xx} and ρ_{xx} are the Hall and the longitudinal resistivity. The single particle model predicts $R_H = 1/ne$ with a singularity at n = 0, whereas experimentally a smooth transition between electrons and holes is observed, representing a coexistence of both carrier types in the transition region.[24] Thus, in devices G1 and H3 we obtain mixing of the carrier concentrations in the range of 89×10^{10} cm^{-2} and 41×10^{10} cm^{-2}, respectively. As at low carrier concentrations graphene mobility is limited by scattering on the charged impurities,[25] higher mobility values for H-devices in comparison to G-devices correlate with the lower residual carrier concentrations. It is peculiar that H-devices show a continuous decrease of the mobility with increasing carrier concentration beyond the electron-hole puddle ranges (see Figure 3d), whereas the mobility of G-devices stays nearly constant. We attribute this behavior to the encapsulation of graphene in H-devices with an about 1 nm thin dielectric sheet terminated with polar amino groups and sulfur species,[16] which effectively screen[26] the charge impurities and suppresses scattering of the electrical carriers. A similar behavior was recently theoretically discussed for top-gated graphene devices with ultrathin gate dielectric layers.[27]

In the following we demonstrate that at low temperatures the magneto-transport properties of H-devices reproduce very well the quantum mechanical phenomena attributed to SLG, **Figure 4**. Thus, Figure 4a shows an evaluation of the Shubnikov-de Haas oscillations with their onset at about 3 T. From the oscillations period we find the hole concentration of 2.3×10^{12} cm^{-2}, which perfectly corresponds to the value set by the back gate voltage U_{BG}. Moreover, at low magnetic fields a conductivity change due to the weak localization effect[28] is clearly observed (see inset to Figure 3a). We applied the weak localization theory[28,29] to perform fitting of these data (blue solid line) and to estimate scattering parameters. The obtained values for phase breaking, intervalley scattering and intravalley scattering times are $\tau\varphi$ = 5.6 ps, τ_i = 0.5 ps, and τ_* = 6 fs, respectively; and the corresponding lengths are $l\varphi$ = 370 nm, l_i = 115 nm, and l_* = 37 nm. These results are in good agreement with the scattering parameters of other transport studies of CVD graphene on silicon oxide substrates.[30] At a high magnetic field the quantum Hall effect (QHE) in device H3 appears as a sequence of plateaus accompanied by the longitudinal resistance oscillations (Figure 4b). The Hall conductivity (Figure 4c)

© 2014 WILEY-VCH Verlag GmbH & Co. KGaA, Weinheim

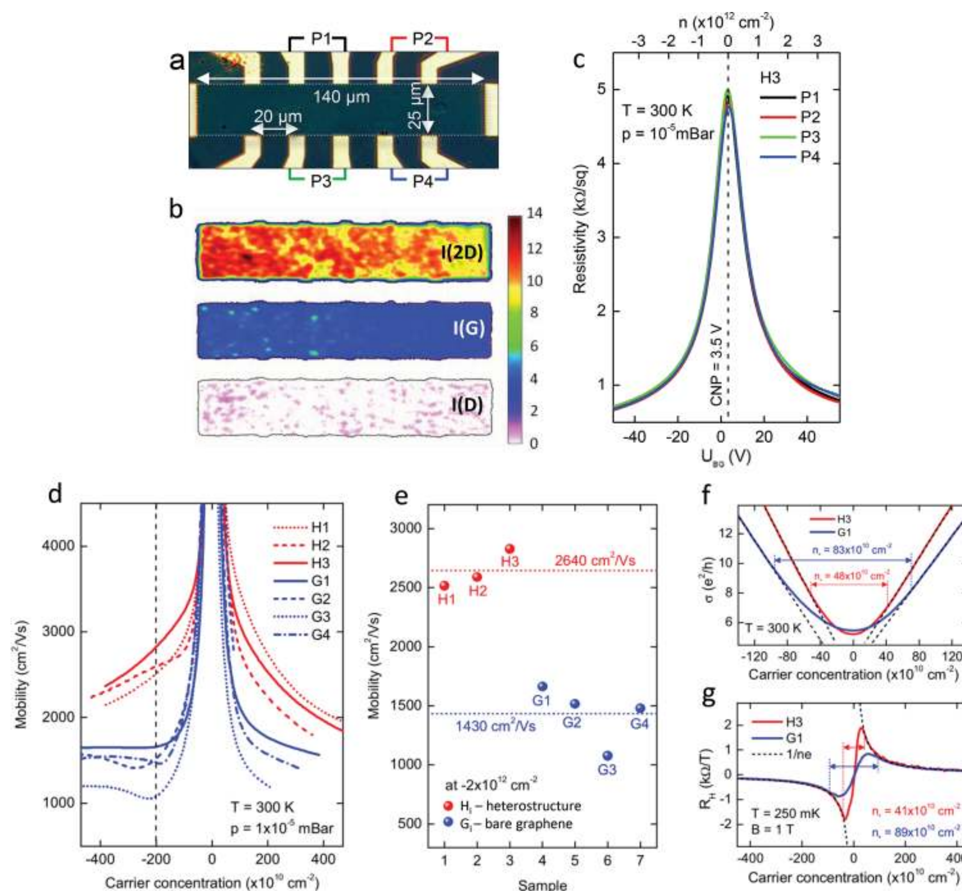

Figure 3. Electric transport measurements of bare graphene (G) and heterostructure (H) electric field devices. a, Optical microscope image of the fabricated H-device. b, Raman spectroscopy maps (λ = 532 nm) of the intensity of the characteristic 2D, G and D peaks. c, RT graphene resistivity at different side contacts (P1-P4) as a function of back-gate voltage, U_{BG}. d, RT electric charge mobility of graphene in H- and G-devices as a function of carrier concentration, *n*. e, Comparison of the RT electric charge mobility in H- and G-devices at $n = -2 \times 10^{12}$ cm^{-2}. f, RT conductivity of graphene in H3 and G1 in the vicinity of their charge neutrality points (CNPs). g, Electrons and holes coexistence revealed by Hall coefficient measurements for devices H3 and G1 at a magnetic field of 1T and a temperature of 250 mK. Dashed lines correspond to the single-particle model for holes and electrons.

follows a staircase shape with $4e^2/h$ high steps, as expected for SLG. Figure 4d presents the QHE in the vicinity of the filling factor $\nu = -2$ in more detail. We observe a vanishing of the longitudinal resistance, which is indicated in a fully developed quantum Hall resistance plateau. In the range of minimum longitudinal resistance the mean value of the relative Hall resistance deviation, δ_r, (see also figure caption to Figure 4d for details) yields a value of only $(-3.5 \pm 3.7) \times 10^{-5}$. To the best of our knowledge, this is the most precise QHE measurement on CVD graphene reported so far. Thus, the magneto-transport measurements unambiguously demonstrate that the intrinsic quality of graphene is preserved in the fabricated NH_2-CNM/SLG vdW heterostructure and that the chemical functionalization of SLG has been achieved in a non-destructive manner.

To test the heterostructures for possible sensor applications, we exposed H-devices to Millipore water at ambient conditions and measured their electrical response. NH_2-CNM sheets insulate the underlying graphene from water[11] and therefore the graphene resistivity can only be affected by a change in the electrostatic environment at the NH_2-CNM/water interface. A special care was taken to prevent the forming of water bridges between gold bonding wires of the devices (see SI for details). Water droplets (see inset to **Figure 5**b) were placed on the heterostructure area using a micropipette, and after the measurements they were then blown away by purging nitrogen. Figure 5a shows the ambipolar electric field effect of the same H-device at ambient conditions and in water. The presence of water results in n-doping of graphene and a shift of the CNP by about 27 V. We attribute this change to the protonation of amino groups ($-NH_3^+$) in NH_2-CNM, which result in an effective gating of graphene through the 1 nm thick dielectric layer of cross-linked biphenylthiols. As estimated from these data, a charge carrier injection into graphene corresponds to a carrier density change of ~2×10^{12} cm^{-2}. With the dielectric constant of NH_2-CNMs ($\varepsilon \approx 2.9$, Ref. [10]) and using the plate capacitor model, we obtain an effective interfacial potential at the water/NH_2-CNM interface of ~120 mV (see SI, p. 5). Figure 5b shows the corresponding dynamic response of the device resistivity acquired by four point measurements with a direct current of 1 μA and U_{BG} = 0 V. Just after placing the first water droplet (green arrow), which only partially covered the heterostructure area, a noticeable and rapid change of the resistivity was detected. After the full coverage with water (red arrow) we measured a giant increase by at least 400% of the graphene

© 2014 WILEY-VCH Verlag GmbH & Co. KGaA, Weinheim
Adv. Mater. 2014,
DOI: 10.1002/adma.201400948

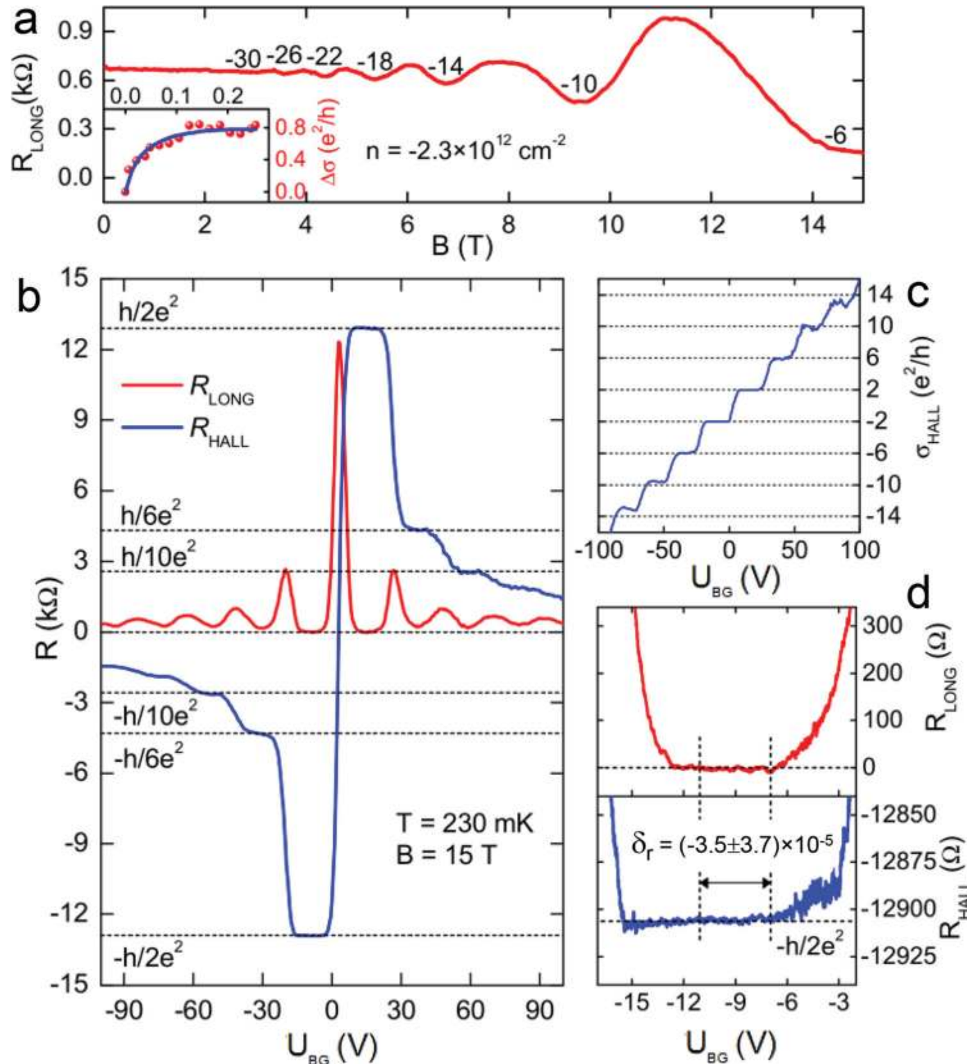

Figure 4. Magneto-transport measurements of the heterostructure device at low temperature (H3, T = 230 mK). a, Shubnikov-de Haas oscillations in graphene with the corresponding filling factors as a function of magnetic field. The inset presents the weak localization effect in graphene at a low magnetic field. Data points are a conductivity change with respect to the zero magnetic field, whereas a blue solid line is a fitting curve from the weak-localization theory. b, The quantum Hall effect as a function of back-gate voltage at $B = 15$ T. Red and blue plots show the longitudinal and Hall resistances, respectively. Horizontal dashed lines correspond to the theoretical quantum resistance plateaus for SLG. c, Hall conductivity calculated as $\sigma_{HALL} = \rho_{HALL}/(\rho_{HALL}^2 + \rho_{LONG}^2)$, where $\rho_{HALL} = R_{HALL}$, $\rho_{LONG} = R_{LONG} \times w/l$, w is a Hall bar width, and l is a distance between voltage probing contacts. d, Detailed investigation of the plateau for the filling factor $\nu = -2$. The upper plot shows vanishing of the longitudinal resistance, and the lower plot shows precise coincidence of the measured quantum Hall resistance with the theoretical value of $-h/2e^2$, where h and e are Planck's constant and electronic charge value, respectively. The relative Hall resistance difference δ_r is defined as $\delta_r = (R_{HALL} - R_K/\nu) / R_K/\nu$ and yields only $(-3.5 \pm 3.7) \times 10^{-5}$.

resistivity, which corresponds to a decrease of the charge carrier concentration in agreement with the ambipolar electric-field effect presented in Figure 5a. Blowing the droplet away (black arrow) results in a fast recovering of the resistivity to its initial value of ~1.6 kΩ/sq. Some instability of the resistivity signal in water was caused by the evaporation and droplet movement, which was observed in an optical microscope.

In summary we have demonstrated the fabrication and characterization of all-carbon NH_2-CNM/SLG heterostructures in which the terminal amino groups are separated by an only 1 nm thick carbon-based dielectric film from the plane of graphene. The intrinsic quality of the SLG sheets is not disturbed by this functionalization; moreover, NH_2-CNMs acts as the effective encapsulation layer improving the electric transport. As the amino groups can further be flexibly chemically functionalized,[16,20] the suggested route opens broad avenues for the engineering of functional electronic devices (e.g., nanosensors). The electric response of the heterostructure devices to water shows the viability of this approach. As CNMs can economically be produced on large scale from a variety of aromatic monolayers,[12] it is promising to use them in the graphene-based electronics as complementary 2D dielectric, similar to hexagonal boron nitride sheets, for the engineering the efficient top-gate electrodes or for making the field-effect tunneling transistors.[31] An additional interesting opportunity is provided by the fact that CNMs can be converted into high electronic quality

© 2014 WILEY-VCH Verlag GmbH & Co. KGaA, Weinheim

COMMUNICATION

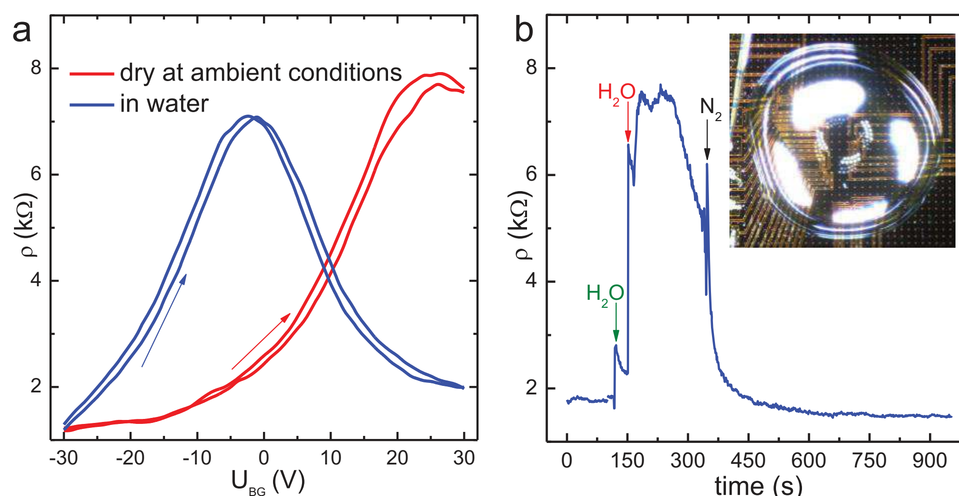

Figure 5. Response of the heterostructure devices to water environment. a, The electric field-effect for a H-device at ambient conditions and with a water droplet on the heterostructure area, see inset in (b); arrows indicate the direction of voltage scans. At ambient conditions and in water a hysteresis in the gate effect between the subsequent opposite direction gate voltage scans was observed with a magnitude of 10 V and 20 V, respectively. This effect is most likely coursed by the trapped charges in devices at these conditions. b, Dynamic electrical response of the device upon placing and removing a water droplet on the heterostructures area (see main text for more details).

graphene by annealing.[32] In this way both graphene and insulating CNMs can be prepared from the same molecular precursor facilitating implementation of all-carbon electronics in nanotechnology.

Supporting Information

This material contains the detailed description of materials and methods, analysis of Raman spectroscopy and microscopy data, atomic force microscopy (AFM) images of bare graphene and heterostructure Hall bar devices, model calculations.

Acknowledgements

This work was supported by the Deutsche Forschungsgemeinschaft (SPP „Graphene“, TU149/2–1, TU149/2–2 and WE3654/3–1; and Heisenberg Programme, TU149/3–1) and the EMRP project „GraphOhm“ (The EMRP is jointly funded by the EMRP participating countries within EURAMET and European Union).

Received: February 28, 2014
Revised: April 8, 2014
Published online:

[1] R. Stine, S. P. Mulvaney, J. T. Robinson, C. R. Tamanaha, P. E. Sheehan, *Anal. Chem.* **2013**, *85*, 509–521.
[2] S. X. Wu, Q. Y. He, C. L. Tan, Y. D. Wang, H. Zhang, *Small* **2013**, *9*, 1160–1172.
[3] T. Kuila, S. Bose, A. K. MishraK. Mishra, P. Khanra, N. H. Kim, J. H. Lee, *Prog. Mater. Sci.* **2012**, *57*, 1061–1105.
[4] H. Y. Mao, Y. H. Lu, J. D. Lin, S. Zhong, A. T. S. Wee, W. Chen, *Prog. Surf. Sci.* **2013**, *88*, 132–159.
[5] A. A. Balandin, *Nat. Mater.* **2011**, *10*, 569–581.
[6] D. R. Dreyer, S. Park, C. W. Bielawski, R. S. Ruoff, *Chem. Soc. Rev.* **2010**, *39*, 228–240.
[7] M. Steenackers, A. M. Gigler, N. Zhang, F. Deubel, M. Seifert, L. H. Hess, C. Lim, K. P. Loh, J. A. Garrido, R. Jordan, M. Stutzmann, I. D. Sharp, *J. Am. Chem. Soc.* **2011**, *133*, 10490–10498.
[8] E. Bekyarova, M. E. Itkis, P. Ramesh, C. Berger, M. Sprinkle, W. A. de Heer, R. C. Haddon, *J. Am. Chem. Soc.* **2009**, *131*, 1336–1337.
[9] Y. Xu, L. Zhao, H. Bai Bai, W. Hong, C. Li, G. Shi, *J. Am. Chem. Soc.* **2009**, *131*, 13490–13497.
[10] C. T. Nottbohm, A. Turchanin, A. Beyer, R. Stosch, A. Gölzhäuser, *Small* **2011**, *7*, 874–883.
[11] A. Turchanin, A. Gölzhäuser, *Prog. Surf. Sci.* **2012**, *87*, 108–162.
[12] P. Angelova, H. Vieker, N.-E. Weber, D. Matei, O. Reimer, I. Meier, S. Kurasch, J. Biskupek, D. Lorbach, K. Wunderlich, L. Chen, A. Terfort, M. Klapper, K. Müllen, U. Kaiser, A. Gölzhäuser, A. Turchanin, *ACS Nano* **2013**, *7*, 6489–6497.
[13] X. S. Li, W. W. Cai, J. H. An, S. Kim, J. Nah, D. X. Yang, R. Piner, A. Velamakanni, I. Jung, E. Tutuc, S. K. Banerjee, L. Colombo, R. S. Ruoff, *Science* **2009**, *324*, 1312–1314.
[14] W. Eck, V. Stadler, W. Geyer, M. Zharnikov, A. Gölzhäuser, M. Grunze, *Adv. Mater.* **2000**, *12*, 805–808.
[15] M. Schnietz, A. Turchanin, C. T. Nottbohm, A. Beyer, H. H. Solak, P. Hinze, T. Weimann, A. Gölzhäuser, *Small* **2009**, *5*, 2651–2655.
[16] Z. Zheng, C. T. Nottbohm, A. Turchanin, H. Muzik, A. Beyer, M. Heilemann, M. Sauer, A. Gölzhäuser, *Angew. Chem. Int. Ed.* **2010**, *49*, 8493–8497.
[17] A. Turchanin, D. Käfer, M. El-Desawy, C. Wöll, G. Witte, A. Gölzhäuser, *Langmuir* **2009**, *25*, 7342–7352.
[18] A. Turchanin, A. Beyer, C. T. Nottbohm, X. Zhang, R. Stosch, A. S. Sologubenko, J. Mayer, P. Hinze, T. Weimann, A. Gölzhäuser, *Adv. Mater.* **2009**, *21*, 1233–1237.
[19] A. Pirkle, J. Chan, A. Venugopal, D. Hinojos, C. W. Magnuson, S. McDonnell, L. Colombo, E. M. Vogel, R. S. Ruoff, R. M. Wallace, *Appl. Phys. Lett.* **2011**, *99*, 122108.
[20] A. Turchanin, A. Tinazli, M. El-Desawy, H. Großmann, M. Schnietz, H. H. Solak, R. Tampé, A. Gölzhäuser, *Adv. Mater.* **2008**, *20*, 471–477.

© 2014 WILEY-VCH Verlag GmbH & Co. KGaA, Weinheim

DOI: 10.1002/adma.201400948

[21] P. Blake, E. W. Hill, A. H. C. Neto, K. S. Novoselov, D. Jiang, R. Yang, T. J. Booth, A. K. Geim, *Appl. Phys. Lett.* **2007**, *91*, 063124.
[22] A. C. Ferrari, D. M. Basko, *Nat. Nanotech.* **2013**, *8*, 235–246.
[23] E. H. Hwang, S. Adam, S. Das Sarma, *Phys. Rev. Lett.* **2007**, *98*, 186806.
[24] S. Wiedmann, H. J. van Elferen, E. V. Kurganova, M. I. Katsnelson, A. J. M. Giesbers, A. Veligura, B. J. van Wees, R. V. Gorbachev, K. S. Novoselov, J. C. Maan, U. Zeitler, *Phys. Rev. B* **2011**, *84*, 115314.
[25] A. S. Mayorov, D. C. Elias, I. S. Mukhin, S. V. Morozov, L. A. Ponomarenko, K. S. Novoselov, A. K. Geim, R. V. Gorbachev, *Nano Lett.* **2012**, *12*, 4629–4634.
[26] F. Chen, J. L. Xia, D. K. Ferry, N. J. Tao, *Nano Lett.* **2009**, *9*, 2571–2574.
[27] Z. Y. Ong, M. V. Fischetti, *Phys. Rev. B* **2012**, *86*, 121409.
[28] E. McCann, K. Kechedzhi, V. I. Fal'ko, H. Suzuura, T. Ando, B. L. Altshuler, *Phys. Rev. Lett.* **2006**, *97*, 146805.
[29] F. V. Tikhonenko, D. W. Horsell, R. V. Gorbachev, A. K. Savchenko, *Phys. Rev. Lett.* **2008**, *100*, 056802.
[30] L. A. Jauregui, H. L. Cao, W. Wu, Q. K. Yu, Y. P. Chen, *Sol. St. Comm.* **2011**, *151*, 1100–1104.
[31] L. Britnell, R. V. Gorbachev, R. Jalil, B. D. Belle, F. Schedin, A. Mishchenko, T. Georgiou, M. I. Katsnelson, L. Eaves, L. S. V. Morozov, N. M. R. Peres, J. Leist, A. K. Geim, K. S. Novoselov, L. A. Ponomarenko, *Science* **2012**, *335*, 947–950.
[32] D. G. Matei, N.-E. Weber, S. Kurasch, S. Wundrack, M. Woszczyna, M. Grothe, T. Weimann, F. Ahlers, R. Stosch, U. Kaiser, A. Turchanin, *Adv. Mater.* **2013**, *25*, 4146–4151.

© 2014 WILEY-VCH Verlag GmbH & Co. KGaA, Weinheim